

Accepted Manuscript

Title: Modelling of thermal fluid dynamics for fusion welding

Author: Chinnapat Panwisawas Yogesh Sovani Richard P. Turner Jeffery W. Brooks Hector C. Basoalto Isabelle Choquet



PII: S0924-0136(17)30418-1
DOI: <http://dx.doi.org/doi:10.1016/j.jmatprotec.2017.09.019>
Reference: PROTEC 15396

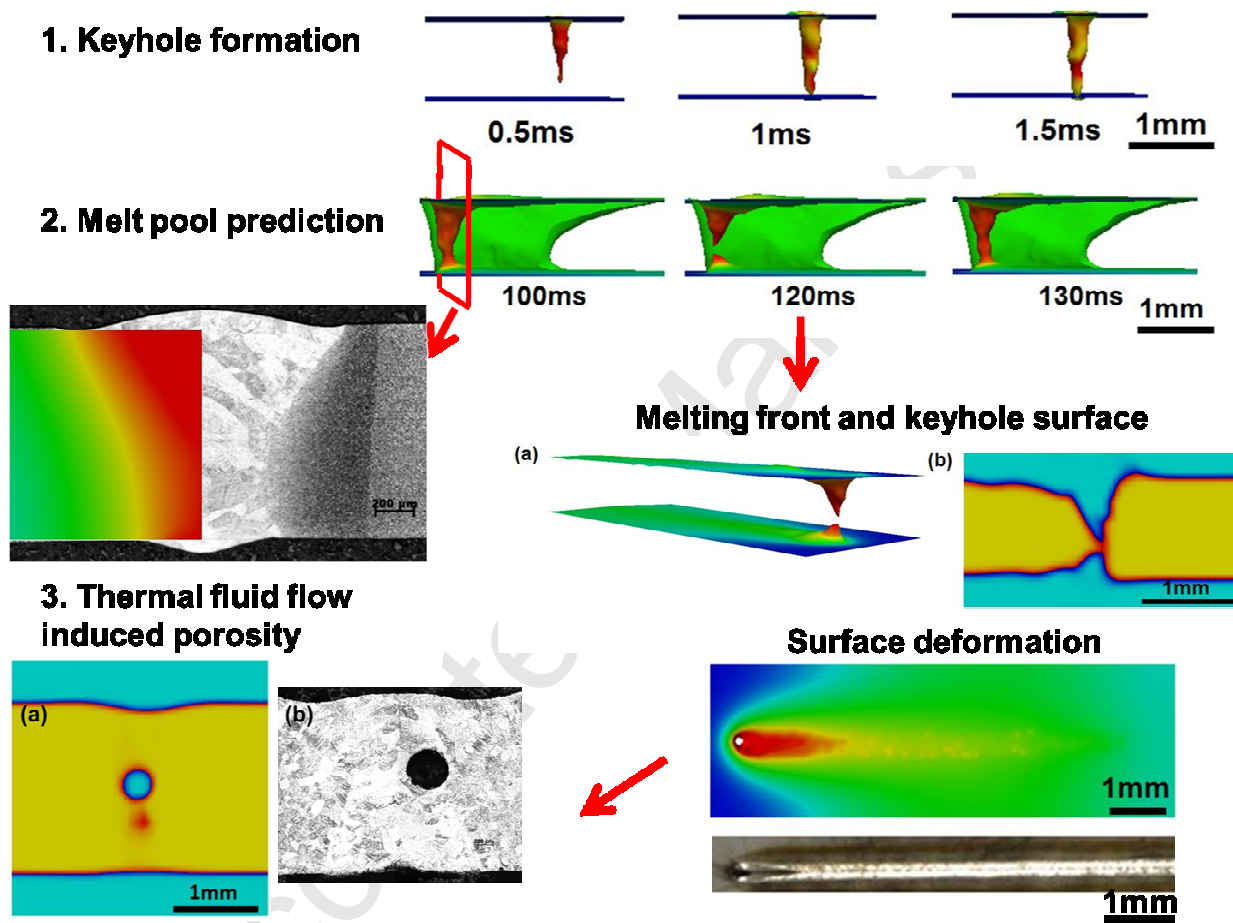
To appear in: *Journal of Materials Processing Technology*

Received date: 8-4-2017
Revised date: 7-9-2017
Accepted date: 9-9-2017

Please cite this article as: Chinnapat Panwisawas, Yogesh Sovani, Richard P. Turner, Jeffery W. Brooks, Hector C. Basoalto, Isabelle Choquet, Modelling of thermal fluid dynamics for fusion welding, *Journal of Materials Processing Tech.* (2017), <http://dx.doi.org/10.1016/j.jmatprotec.2017.09.019>

This is a PDF file of an unedited manuscript that has been accepted for publication. As a service to our customers we are providing this early version of the manuscript. The manuscript will undergo copyediting, typesetting, and review of the resulting proof before it is published in its final form. Please note that during the production process errors may be discovered which could affect the content, and all legal disclaimers that apply to the journal pertain.

Graphical Abstract



Modelling of thermal fluid dynamics for fusion welding

Chinnapat Panwisawas*, Yogesh Sovani, Richard P. Turner, Jeffery W. Brooks,
Hector C. Basoalto*

*School of Metallurgy and Materials, University of Birmingham, Edgbaston, Birmingham
B15 2TT, UK*

Isabelle Choquet

Department of Engineering Science, University West, 461 86 Trollhättan, Sweden

Abstract

A fluid dynamics approach to modelling of fusion welding in titanium alloys is proposed. The model considers the temporal and spatial evolution of liquid metal/gas interface to capture the transient physical effects during the heat source-material interaction of a fusion welding process. Melting and vaporisation have been considered through simulation of all interfacial phenomena such as surface tension, Marangoni force and recoil pressure. The evolution of the metallic (solid and liquid) and gaseous phases which are induced by the process enables the formation of the keyhole, keyhole dynamics, and the fully developed weld pool geometry. This enables the likelihood of fluid flow-induced porosity to be predicted. These features are all a function of process parameters and formulated as time-dependent phenomena. The proposed modelling framework can be utilised as a simulation tool to further develop understanding of defect formation such as weld-induced porosity for a particular fusion welding application. The modelling results are qualitatively compared with available experimental information.

Keywords: Keyhole modelling, Fusion welding, Thermal fluid dynamics, Titanium alloys

*Corresponding author

Email address: c.panwisawas@bham.ac.uk, h.basoalto@bham.ac.uk ()

1. Introduction

Fusion welding operations have been implemented across a number of industrial applications to fabricate complex components. Computational fluid dynamics (CFD) has proved valuable in capturing weld pool geometries, understanding keyhole formation and prediction of the likelihood for defect formation. Zhang et al. (2013) used experimental techniques to capture in-situ monitoring of welding, and Tan and Shin (2015) simulated the thermal fluid flow coupled with electromagnetic field. In general, emphasis has been placed on steady state solutions of the Navier-Stokes equation. Rai et al. (2007) proposed a model for fluid flow and heat transfer with a heat source moving with respect to the base metal and a pre-defined keyhole surface for Ti-6V-4Al. A latter model was applied to other material systems, see (Rai et al., 2009a). The limitations in these previous studies included analysis with implementing the model using the heat source as a reference frame; therefore it is the base metal that moves. The system of equations was expressed in a moving reference frame. A numerical framework for the simulation of keyhole formation and oscillation, the fully developed weld pool geometry and the porosity obtained using a moving heat source model is required to capture transient and steady state response.

Modelling of fusion welding requires a detailed understanding of all the complex physical phenomena that occurs in the process. Phase changes (i.e. melting and vaporisation) arising during the interaction between the heat source and the material, together with the resulting mechanical forces are the fundamental mechanisms for the formation of a keyhole. The high energy density of the heat source induces vaporisation at the metal surface producing a recoil pressure and a strong thermo-capillary force (Scriven and Sternling, 1960). The high gradient of the melt pool surface temperature drives the flow of the liquid metal outwards and it can affect the keyhole opening. Surface deformation occurs at the liquid/gas interface where the keyhole surface is defined due to the combined effects of the surface tension and hydrostatic force that oppose the recoil pressure as used in Tan et al. (2013). The laser experiences multi-

ple reflections before the beam escapes the cavity (Svenungsson et al., 2015), however as a first approximation the laser heat source can be provided by a three-dimensional (3D) Gaussian distribution.

Geiger et al. (2009) and Koch et al. (2011) have successfully simulated periodic keyhole oscillations using a volume of fluid (VOF) approach. Similarly Otto et al. (2011) has used the VOF method to assess the dynamics of several laser based processes including full penetration welding. Lee et al. (2002) established a two dimensional model of a stationary laser weld using a thermal fluid flow calculation using the VOF method to demonstrate that protrusion occurs on the keyhole wall provoking keyhole collapse and void formation at the bottom of the weld during partial penetration welding. Rai et al. (2007) has developed 3D modelling of keyhole laser welding and later Rai et al. (2009b) modelled electron beam welding in Ti-6Al-4V although solutions for the effects of vaporisation and recoil pressure were not fully integrated in the model. Experimentally, Zhao et al. (2011) investigated keyhole induced porosity in deep penetration laser welding by considering the effects of the plasma gas combined with liquid-solid metal interactions. They concluded that the cause of keyhole induced porosity was bubble formation from keyhole collapse and shrinkage. Keyhole dynamics and instability have also been studied experimentally using high speed camera imaging (Jin et al., 2002), X-ray transmission imaging (Abt et al., 2011) and optical emission spectroscopy (Zhang et al., 2013) to demonstrate that the instability of the keyhole is caused by local temporal fluctuations of evaporation and imbalance between upward and downward flow along the wall of the keyhole cavity.

This paper presents a novel CFD modelling framework capturing the transient behaviour of a dynamic weld pool, in order to couple the processing and metallurgy of fusion welding. A thermal fluid flow model for simulating fusion welding in titanium alloys has been implemented using C++ open source Open Field Operation and Manipulation (OpenFOAM®) toolbox to capture the physical effects arising during both the weld pool formation conditions and in the fully developed weld pool achieved at relatively long welding times of up to 1

second. As a first approximation, it is assumed that the present model is applicable for the conditions investigated neglecting any effects of keyhole bending due to heat source travel speeds.

2. Modelling methodology: Thermal fluid dynamics

In simulating the evolution of a keyhole during welding processes, a three-phase (solid, liquid and vapour) model comprising of incompressible, non-isothermal immiscible fluids corresponding to the alloy and surrounding gaseous phase is considered. For the latter no distinction between ambient air and metallic vapour is made within the current framework. Note that the mass source of metallic vapor is not modeled. A VOF interface capturing approach was used to track evolution during the process. For process conditions of interest the maximum velocities of the molten alloy are less than Mach 0.5, and as a result flows are expected to be laminar. It is also assumed that the gas phase is laminar. Therefore constitutive behaviour of the fluids is assumed to be Newtonian (Landau and Lifshitz, 2010). Marangoni force or thermo-capillary force are accounted for in the model and assume a temperature dependent surface tension. Vaporisation is considered using an empirical model following the approach reported by Courtois et al. (2013) without considering a physics-based kinetic Knudsen layer at the liquid-vapour interface. The semi-empirical model of laser heat source has been adopted from Xu et al. (2011) to mimic the shape of a keyhole assuming that the beam intensity decreases linearly when moving down into the keyhole. It does not take into account the multiple reflections. The model takes into account the latent heat of fusion and evaporation adopted the approach reported in Voller et al. (1987). The inter-dendritic fluid flow in the mushy zone at the solid-liquid interface has been calculated via a sink term, the so-called Darcy's term, at the macroscopic scale. Darcy's term is only a numerical viscosity allowing for the description of the metal with the Navier-Stokes equation in both the liquid and the solid phases. It is only used here to create an artificial (a numerical) friction to force the metal to stop flowing in

locations where it is in solid state. Thermophysical properties are assumed to be constant in both metallic and gaseous phases, due to the lack of information of temperature dependence of liquid metal and metallic vapour.

To model the dynamics of the metallic-gaseous interface, it is required to define the metallic phase α_1 (i.e. either solid metal or liquid metal) and gas phase α_2 in which they follow

$$\alpha_1 + \alpha_2 = 1 \quad (1)$$

The volume of fluid method is used to track the liquid-gas interface movement by solving the following advection equation for the α_1 phase driven by an effective velocity \mathbf{u} ,

$$\frac{\partial \alpha_1}{\partial t} + \nabla \cdot (\alpha_1 \mathbf{u}) = -\frac{\dot{m}_{\text{vap}}}{\rho_2} \quad (2)$$

$$\mathbf{u} = \alpha_1 \mathbf{u}_1 + \alpha_2 \mathbf{u}_2 \quad (3)$$

where a sink term $-\frac{\dot{m}_{\text{vap}}}{\rho_2}$ has been included to account for the effect of evaporation on the location of the free surface. The mass evaporation rate \dot{m}_{vap} is defined later. Combining Equations (1)-(3) gives the following differential equation governing the evolution of the α_1 interface,

$$\frac{\partial \alpha_1}{\partial t} + \nabla \cdot (\alpha_1 \mathbf{u}_1) + \nabla \cdot ((1 - \alpha_1) \alpha_1 \mathbf{u}_r) = -\frac{\dot{m}_{\text{vap}}}{\rho_2} \quad (4)$$

where $\mathbf{u}_r = \mathbf{u}_2 - \mathbf{u}_1$ is the relative (physical compression) velocity between two phases and is only active in the interface cells, owing to the term $(1 - \alpha_1)\alpha_1$.

In a similar manner, mass conservation for a compressible fluid can be expressed as,

$$\frac{\partial \bar{\rho}}{\partial t} + \nabla \cdot (\bar{\rho} \mathbf{u}) = 0 \quad (5)$$

where $\bar{\rho} = \rho_1 \alpha_1 + \rho_2 \alpha_2$. Note that the mass source term of metallic vapour is neglected in the gas phase.

Momentum conservation is the Navier-Stokes equation:

$$\frac{\partial \bar{\rho} \mathbf{u}}{\partial t} + \nabla \cdot (\bar{\rho} \mathbf{u} \otimes \mathbf{u}) = \nabla \cdot \mathbf{S} + \mathbf{F}_{\text{body}} + \mathbf{f}_{\text{surface}} \quad (6)$$

where \mathbf{S} is the stress tensor, \mathbf{F}_{body} the body force and $\mathbf{f}_{\text{surface}}$ the force acting on the fluid/gas interface. The \mathbf{S} is defined by a (hydrostatic) pressure term, p , and the (deviatoric) stress tensor, \mathbf{T} ,

$$\mathbf{S} = -p\mathbb{I} + \mathbf{T} \quad (7)$$

and the viscous stress tensor is expressed as

$$\mathbf{T} = 2\bar{\mu} \left[\left(\frac{1}{2} \nabla \mathbf{u} + \frac{1}{2} (\nabla \mathbf{u})^T \right) - \frac{1}{3} (\nabla \cdot \mathbf{u}) \mathbb{I} \right] \quad (8)$$

where $\bar{\mu}$ is the dynamic viscosity. Contributions to \mathbf{F}_{body} come from the buoyancy, $\mathbf{F}_{\text{buoyancy}}$, and Darcy's terms associated with temperature variations and viscosity changes due to melting, $\mathbf{F}_{\text{Darcy}}$,

$$\mathbf{F}_{\text{body}} = \mathbf{F}_{\text{buoyancy}} + \mathbf{F}_{\text{Darcy}} \quad (9)$$

The buoyancy-driven flow term arises from density differences and will be assumed to be approximated by the Boussinesq relation,

$$\mathbf{F}_{\text{buoyancy}} = \bar{\rho} g \hat{\mathbf{e}}_z \beta (T - T_{\text{ref}}) \quad (10)$$

where T is the temperature, T_{ref} is a reference temperature, g is the magnitude of the gravitational acceleration, $\hat{\mathbf{e}}_z$ is a gravitational unit vector and β is the thermal expansion coefficient. The Darcy damping force term which takes into account frictional dissipation in the mushy zone is calculated by making use of the Carman-Kozeny equation and is applied only in the solid region of the metallic phase α_1 ,

$$\mathbf{F}_{\text{Darcy}} = -\alpha_1 K_{CK} \left(\frac{(1 - f_L)^2}{f_L^3 + C_{CK}} \right) \mathbf{u} \quad (11)$$

where K_{CK} is the permeability coefficient and C_{CK} is a small numerical constant. If a non-isothermal phase change has taken place, the metallic liquid fraction can be derived using an error function as defined in Rösler and Brüggemann (2011)

$$f_L = \frac{1}{2} \text{erf} \left(4 \frac{T - T_m}{T_l - T_s} \right) + \frac{1}{2} \quad (12)$$

with the melting temperature T_m , the arithmetic mean between liquidus temperature T_l and solidus temperature T_s . The continuous liquid fraction Equation 12 would provide directly its coupling between the liquid fraction and the energy conservation equation and a smooth phase change. The temporal and spatial gradients of the continuous liquid fraction will be assumed to evolve through the following differential equations from Rösler and Brüggemann (2011),

$$\frac{\partial f_L}{\partial t} = \xi \frac{\partial T}{\partial t}, \quad \nabla f_L = \xi \nabla T$$

where

$$\xi = \frac{4}{\sqrt{\pi}(T_l - T_s)} \exp \left(16 \left(\frac{T - T_m}{T_l - T_s} \right)^2 \right)$$

The interfacial phenomena taken into account in this work are the surface tension or capillary force, $\mathbf{f}_{\text{surface tension}}$, Marangoni force or thermo-capillary force $\mathbf{f}_{\text{Marangoni}}$ and recoil pressure $\mathbf{f}_{\text{recoil}}$. The total surface force is then given by,

$$\mathbf{f}_{\text{surface}} = (\mathbf{f}_{\text{surface tension}} + \mathbf{f}_{\text{Marangoni}} + \mathbf{f}_{\text{recoil}})\delta. \quad (13)$$

where the parameter δ ensures that the surface forces contributing to $\mathbf{f}_{\text{surface}}$ are only applied to the liquid-gas interface (Brackbill et al., 1992) and Sun and Beckermann (2004) is defined as:

$$\delta = |\nabla \alpha_1| \cdot \frac{2\bar{\rho}}{(\rho_1 + \rho_2)} \quad (14)$$

The $2\bar{\rho}/(\rho_1 + \rho_2)$ factor is a harmonic damping term that is used to smear out the effect between low and high density phases. The surface force per unit interfacial area $\mathbf{f}_{\text{surface tension}}$ is written as (Brackbill et al., 1992)

$$\mathbf{f}_{\text{surface tension}} = \sigma \kappa \hat{\mathbf{n}} \quad (15)$$

where σ is the surface tension and κ the local curvature of the surface with unit normal $\hat{\mathbf{n}} = \nabla \alpha_1 / |\nabla \alpha_1|$.

The temperature dependence of the the surface tension results in the Marangoni force, after Scriven and Sternling (1960), given by (Saldi, 2012),

$$\mathbf{f}_{\text{Marangoni}} = \frac{d\sigma}{dT} (\nabla T - \hat{\mathbf{n}}(\hat{\mathbf{n}} \cdot \nabla T)) \quad (16)$$

The liquid-vapour interface can be modelled here via the thermo-capillary effect and recoil pressure p_{recoil} which gives a force $\mathbf{f}_{\text{recoil}}$ on the liquid/vapour interface,

$$\mathbf{f}_{\text{recoil}} = -\hat{\mathbf{n}}((p_{\text{recoil}}(\mathbf{x})\mathbf{I}) \cdot \hat{\mathbf{n}}) \quad (17)$$

In the present work, a simpler recoil pressure model adopted from Courtois et al. (2013) which first derived from the Clausius-Clapeyron equation (Ytrehus and Østomo, 1996) has been used to simulate the effect,

$$p_{\text{recoil}} = p_0 \exp \left\{ \frac{m_{\text{mol}} h_{\text{vap}}}{R} \left(\frac{1}{T_{\text{vap}}} - \frac{1}{T} \right) \right\} \quad (18)$$

where T_{vap} , h_{vap} , m_{mol} and p_0 are vaporization temperature, enthalpy of vaporisation, molar mass and vapor pressure at the boiling temperature T_{vap} , respectively. Here, the \dot{m}_{vap} can be defined as (Geiger et al., 2009):

$$\dot{m}_{\text{vap}} = -\alpha_1 \alpha_2 p_{\text{recoil}} \sqrt{\frac{m_{\text{mol}}}{2\pi RT}} \quad (19)$$

The evaporation rate is the rate per unit area that only applies on the region containing both α_1 and α_2 phases.

The rate of change of total energy of the systems (internal plus kinetic energy) of the system can be expressed in terms of the heat flux \mathbf{Q} provided by an external source and the work done by surface forces on the interface. It will be assumed that the rate of work done by body and surface forces are small compared with the rate of increase of total energy and the rate of heat flux into the fluid volume V .

In this work, the internal energy or enthalpy e is associated with phase transitions from solid to vapour and can be calculated from the specific heat \bar{C}_p as,

$$e = \begin{cases} \int_{T_{\text{ref}}}^T \bar{C}_p dT, & \text{if } T \leq T_s \\ \int_{T_{\text{ref}}}^T \bar{C}_p dT + h_{\text{melting}}, & \text{if } T_s < T < T_{\text{vap}} \\ \int_{T_{\text{ref}}}^T \bar{C}_p dT + h_{\text{vap}}, & \text{if } T \geq T_{\text{vap}} \end{cases} \quad (20)$$

where $h_{\text{melting}} = f_L L_{\text{melting}}$, T_{vap} and T_s are the evaporation and solidus temperatures, respectively.

To take into account the laser power heat source, the heat density function proposed by Xu et al. (2011) for volumetric heat source $q_{\text{heatSource}}$ is adopted to simulate the heat flux input, where

$$q_{\text{heatSource}} = \frac{3\eta_{\text{laser}}q_{\text{laser}}}{\pi(1-e^{-3})(E+F)} \left(\frac{1-\chi}{z_e-z_i}z + \frac{\chi z_e-z_i}{z_e-z_i} \right) \exp\left(-\frac{3r^2}{r_0^2(z)}\right) \quad (21)$$

$$r_0(z) = \frac{z^2}{p} + s; \quad (22)$$

$$p = \frac{z_e^2 - z_i^2}{r_e - r_i} \quad s = \frac{r_i z_e^2 - r_e z_i^2}{z_e^2 - z_i^2} \quad (23)$$

$$E = \frac{1-\chi}{z_e-z_i} \left\{ \left(\frac{1}{p^2} \frac{z_e^6}{6} + \frac{s}{p} \frac{z_e^4}{2} + \frac{s^2}{2} z_e^2 \right) - \left(\frac{1}{p^2} \frac{z_i^6}{6} + \frac{s}{p} \frac{z_i^4}{2} + \frac{s^2}{2} z_i^2 \right) \right\} \quad (24)$$

$$F = \frac{\chi z_e - z_i}{z_e - z_i} \left\{ \left(\frac{1}{p^2} \frac{z_e^5}{5} + 2 \frac{s}{p} \frac{z_e^3}{3} + s^2 z_e^2 \right) - \left(\frac{1}{p^2} \frac{z_i^5}{5} + 2 \frac{s}{p} \frac{z_i^3}{3} + s^2 z_i^2 \right) \right\} \quad (25)$$

Here, the heat source is a volume (truncated cone) with circular top side initially centered in \mathbf{x}_0 at elevation z_e of top radius r_e and with circular bottom side at elevation z_i of bottom radius r_i ; all of which have to provide into the model to simulate the heat profile. The laser heat source is assumed to be travelling along the y -axis with a uniform velocity v_{beam} and a laser power q_{laser} . Effective absorption coefficient η_{laser} is introduced in the heat source model to account for the interaction of the laser with the weld pool.

Vaporisation, radiation and convection are the phenomena taking place at the liquid-vapour interface. The heat dissipations can be fully calculated using Eq. 20. However, for simplicity, the heat loss due to vaporisation, convection

and radiation decrease the total heat flux input. Therefore, the conservation of total energy becomes

$$\bar{\rho} \frac{D}{Dt} \left(e + \frac{1}{2} u^2 \right) = \nabla \cdot (k \nabla T) + [q_{\text{heatSource}} - q_{\text{vap}}] \cdot \frac{2\bar{\rho}\bar{C}p}{(\rho_1 C p_1 + \rho_2 C p_2)} \quad (26)$$

where $\frac{D}{Dt} \equiv \frac{\partial}{\partial t} + \mathbf{u} \cdot \nabla$ and

$$q_{\text{vap}} = \dot{m}_{\text{vap}} h_{\text{vap}} |\nabla \alpha_1|. \quad (27)$$

Note that in Eq. 26 use has been made of the shape surface force factor $2\bar{\rho}\bar{C}p/(\rho_1 C p_1 + \rho_2 C p_2)$ on the heat source and sink terms to take into account the density difference between metallic and gaseous phases (Sun and Beckermann, 2004).

3. Experimental

Table 1: Chemical composition of Ti-6Al-4V material used in this work (weight percentage).

Alloy	Ti	Al	V	C	Fe	O	N
Ti-6Al-4V	Balance	5.50-6.75	3.50-4.50	0.08	0.30	0.20	0.05

In this study, a bead-on-plate laser weld upon samples of 1 mm thickness plates of Ti-6Al-4V titanium alloy with 2000W laser power and 100mm/s traveling speed and with 4000W laser power and 25mm/s traveling speed was performed using a Trumpf TruDisk laser system, which employs a fiber laser with a wavelength of 1075nm and a beam spot size of 800 μ m in diameter. Ti-6Al-4V alloy plate was provided by Ti-Tek UK Ltd, Birmingham. The target chemical compositions in weight percentage of the Ti-6Al-4V alloy are shown in Table 1. The respective optical micrograph for the welding condition was captured and analysed using the Zeiss Axioskop 2 MAT Optical microscope facility. The system of thermal fluid governing equations is made of Eqs. 2, 5, 6, and 26. Material properties required by the model are adopted from literature Rai et al. (2009a, 2007); Elmer et al. (2004); Boivineau et al. (2006); Li et al. (2006) for

Ti-6Al-4V alloy. The thermodynamic and transport properties are tabulated in Tables 2 and 3.

Table 2: Data used for fluid flow and heat transfer calculations reported by Li et al. (2006); Rai et al. (2007, 2009a).

Physical Properties	Ti-6Al-4V
Solidus temperature, (K)	1878
Liquidus temperature, (K)	1928
Evaporation temperature, (K)	3315
Density of liquid, ($\text{kg} \cdot \text{m}^{-3}$)	4000
Atomic mass, (u)	45.90
Specific heat of solid, ($\text{Jkg}^{-1}\text{K}^{-1}$)	670
Specific heat of liquid, ($\text{Jkg}^{-1}\text{K}^{-1}$)	730
Thermal conductivity of solid, ($\text{Wm}^{-1}\text{K}^{-1}$)	21
Thermal conductivity of liquid, ($\text{Wm}^{-1}\text{K}^{-1}$)	29
Viscosity, ($\text{Pa} \cdot \text{s}$)	0.005
Coefficient of thermal expansion, (K^{-1})	8×10^{-6}
Surface tension coefficient, (Nm^{-1})	1.4
Temperature coefficient of surface tension, ($\text{Nm}^{-1}\text{K}^{-1}$)	-0.26×10^{-3}
Enthalpy of solid at melting point, (Jkg^{-1})	1.12×10^6
Enthalpy of liquid at melting point, (Jkg^{-1})	1.49×10^6
Enthalpy change of evaporation, (Jkg^{-1})	2.7×10^5
Atmospheric pressure, (Nm^{-2})	101300
Ideal gas constant, ($\text{JK}^{-1}\text{mol}^{-1}$)	8.314
Boltzmann's constant, (JK^{-1})	1.38×10^{-24}
Emissivity	0.2
Stefan-Boltzmann constant, ($\text{Wm}^{-2}\text{K}^{-4}$)	5.670×10^{-8}
Heat transfer coefficient, ($\text{Wm}^{-2}\text{K}^{-1}$)	210

Table 3: Data used for heat source model in this calculation.

Parameters	Value
Proportion factor, χ	1.0
Total beam power, (W)	2000 , 4000
Absorption coefficient or absorptivity	0.24
Top Beam radii, (r_e , μm)	200, 300, 400
Top Beam position, (z_e , mm)	1.5
Bottom Beam radii, (r_i , μm)	50
Bottom Beam position, (z_i , mm)	0.5
Beam velocity, (ms^{-1})	0.10 , 0.025

4. Results and Discussion

This section focuses on a numerical study of the solutions to the field of equations governing keyhole dynamics. The following welding conditions have been taken for fusion welding of Ti-6Al-4V: 200, 300 and 400 μm beam radius using a laser power of 2000W and travel speed of 100mm/s, and 400 μm beam radius using a laser power of 4000W and travel speed of 25mm/s. The calculation domain is approximately 1.5 million elements with constant mesh size of 5 μm (using a rectangular plate of dimensions 3mm \times 15mm \times 1mm, surrounded with atmospheric gas).

Figure 1 presents the calculated temperature field at a number of time slices for different laser beam spot sizes. It is shown that the larger the beam radius, the slower the time to full penetration. The model predicts that at least 7ms is required to reach full penetration for the 800 μm beam diameter; whereas only 1.5ms is required for 400 μm beam diameter. The model predicts the development of undulations on the liquid/vapour interface, which arise from temperature variations affecting the recoil pressure at the interface.

Simulation of the keyhole dynamics, once full penetration has been achieved, are now presented. For a 400 μm beam radius weld, the model predicts fluctua-

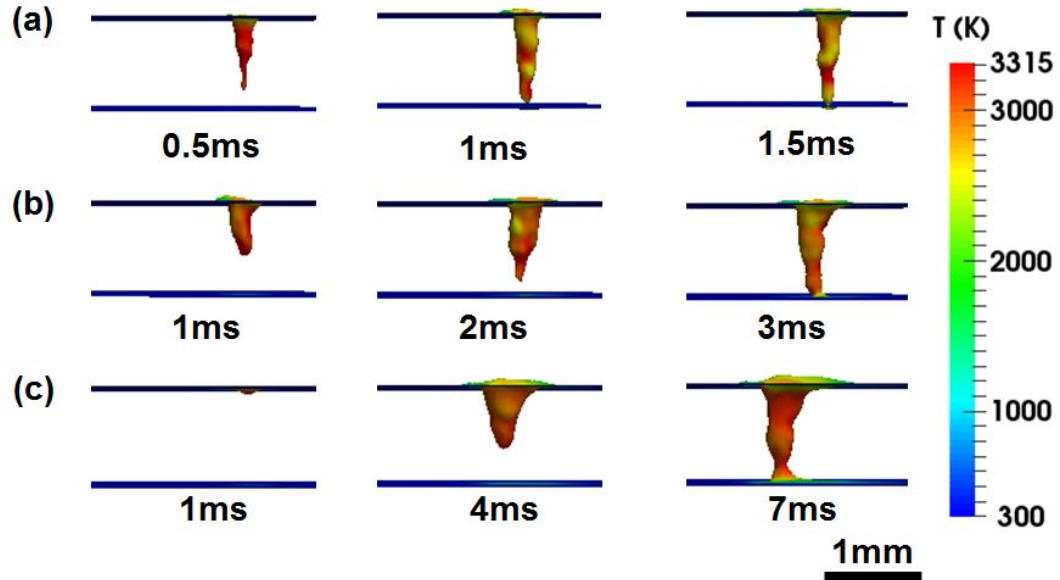


Figure 1: Keyhole formation and time to full penetration of the laser welding with different beam radii: (a) $200\mu\text{m}$, (b) $300\mu\text{m}$, and (c) $400\mu\text{m}$.

tions of the keyhole surface as shown in Fig. 2. During the first 30ms of the weld pool simulation, the outer contour surface grows and becomes fully developed after 40 ms.

However, once the fully developed weld pool condition is reached, local fluctuations of the interface result in predictions of partial collapse of the keyhole surface, e.g. at 120ms.

To the best of the authors' knowledge, this is the first report on predictions of the partial collapse of the keyhole surface (Fig. 3(a)). It is shown that after 120ms of welding time the incomplete collapse keyhole is predicted to show similar features as reported by Huang et al. (2012). For qualitative comparison, Huang et al. (2012) has reported experimentally observed partial collapse of the keyhole surface through 3D X-ray tomography. This is shown in Fig. 3(b) which has similar features as Fig. 3(a). Moreover, the measured melting front thickness, see Fig. 3(d), was approximately $100\mu\text{m}$ which is the same value as the model prediction here in Fig. 3(c).

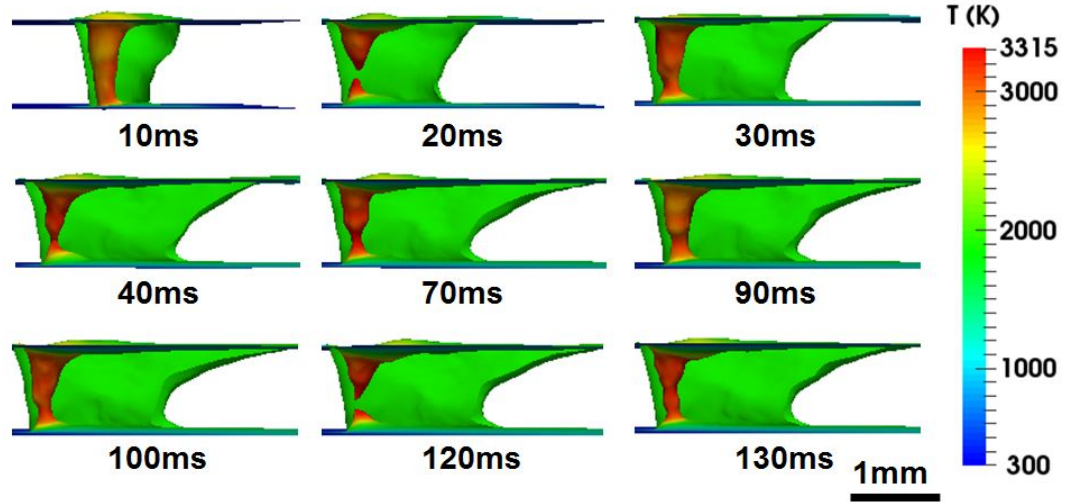


Figure 2: Keyhole oscillation and fully developed weld pool formation of the laser welding with $400\mu\text{m}$ beam radius and 2000 W laser power.

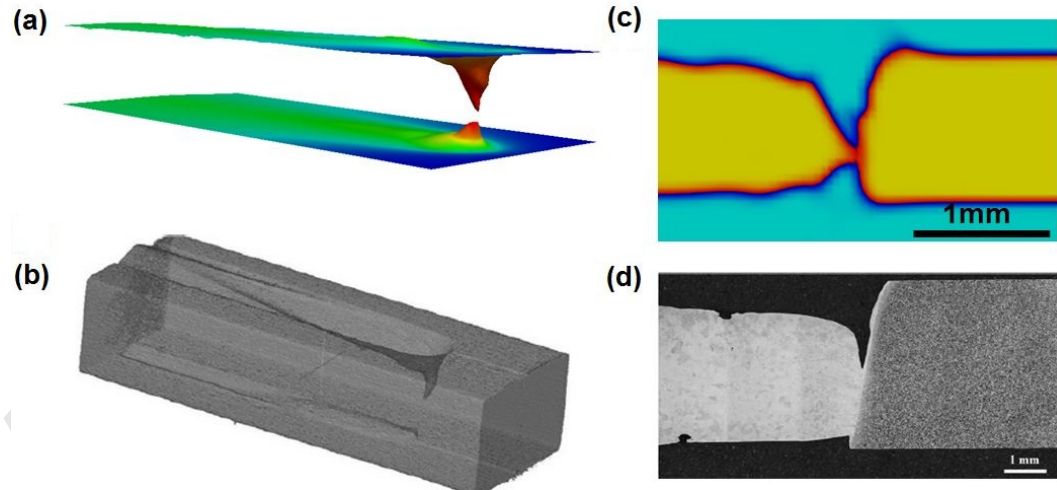


Figure 3: Comparison of captured weld pool shape and melting front: (a) modelling results illustrating the weld pool and incompletely collapsed keyhole qualitatively compared with available X-ray tomography results from fusion weld (b), after Huang et al. (2012), and longitudinal section illustrating the captured melting front from (c) fraction of solid result from modelling, qualitatively compared with the same experiment (d) after Huang et al. (2012).

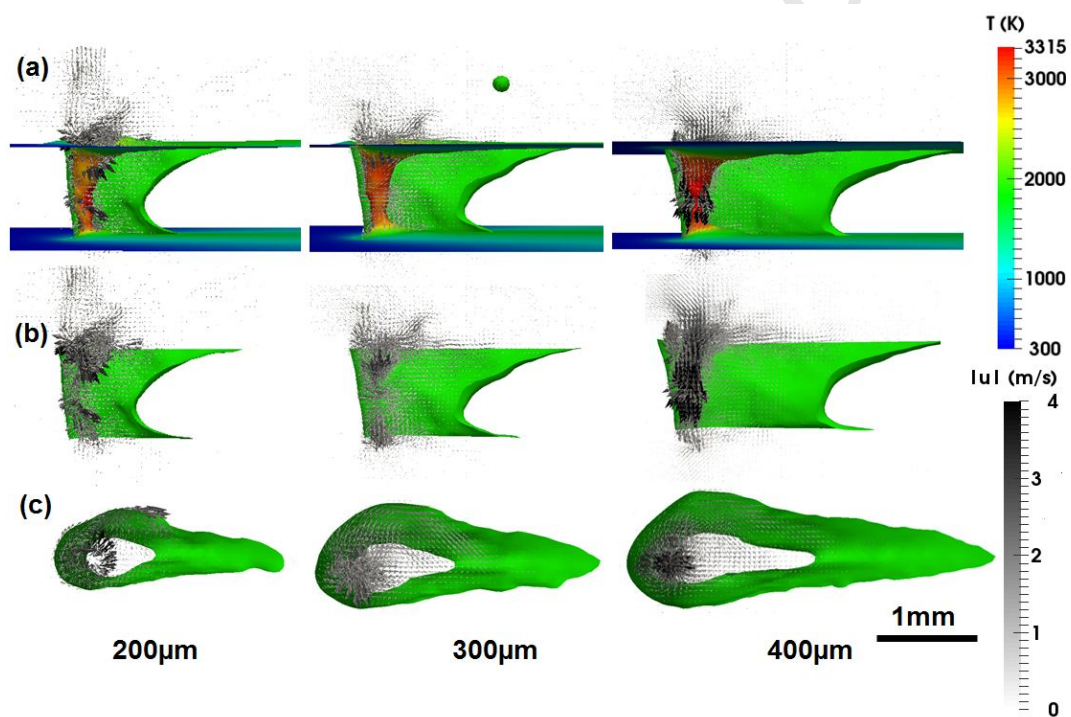


Figure 4: Weld pool dynamics of the steady state weld pool shapes during the laser welding of 2000 W laser power with different beam radii. The results show (a) fluid flow around the keyhole, (b) longitudinal view of weld pool and (c) top view of the melt pool.

Numerical simulations of the liquid metal flow within the melt pool are now presented, which is important in understanding keyhole stability and the formation of process induced pores. Temperature and velocity fields at the liquid/vapour and liquid/solid interfaces are presented in Fig. 4(a) and (b). Undulations on the keyhole surface are predicted which are associated with non-uniform vapour/gas transitions along the interface, seen in Fig.4(a). This may result in a non-planar keyhole interface and subsequent unstable flow behaviour within the weld pool. This could potentially be further understood by considering the multiple reflection and energy absorption.

High flow velocities of the liquid metal are predicted ahead of the keyhole front rather than the trailing side. This is consistent with the spatial distribution of the energy density from the heat source. The model predicts velocity flow lines within the weld pool inducing circular flows around the keyhole surface and these flow lines travel down from the top free surface toward the toe of the weld bead. Moreover, due to variations in temperature within the weld, the flow velocity re-circulates which causes vortices to be formed at the toe, consistent with Fabbro (2010). Such flows can be seen for the $400\mu\text{m}$ beam radius weld simulation shown in Figure 4. It is proposed that such flows may lead to the formation of gas bubbles that may eventually become process induced pores as reported by Huang et al. (2012).

Lateral side flows causing molten material to flow around the vapour phase keyhole are predicted and these are believed to be responsible for the asymmetric weld pool geometry illustrated by the model. Keyhole surface instability swelling due to the vapour impacted heated zone has been experimentally observed (Fabbro, 2010); this phenomena causes the weld pool asymmetry, and the numerical model predicted this effect, a vortex can be seen on one side of the weld (see Fig.4(c)). Occasionally, if the melt dynamic close to the free surface is very unstable, a melt jet (the liquid metal spattering) is to be predicted as shown in Fig. 4(a) for the $300\mu\text{m}$ beam radius weld.

The model gives reasonable predictions of the weld pool shape at the top and the bottom of the weld plate as demonstrated in Fig. 5. The simulated

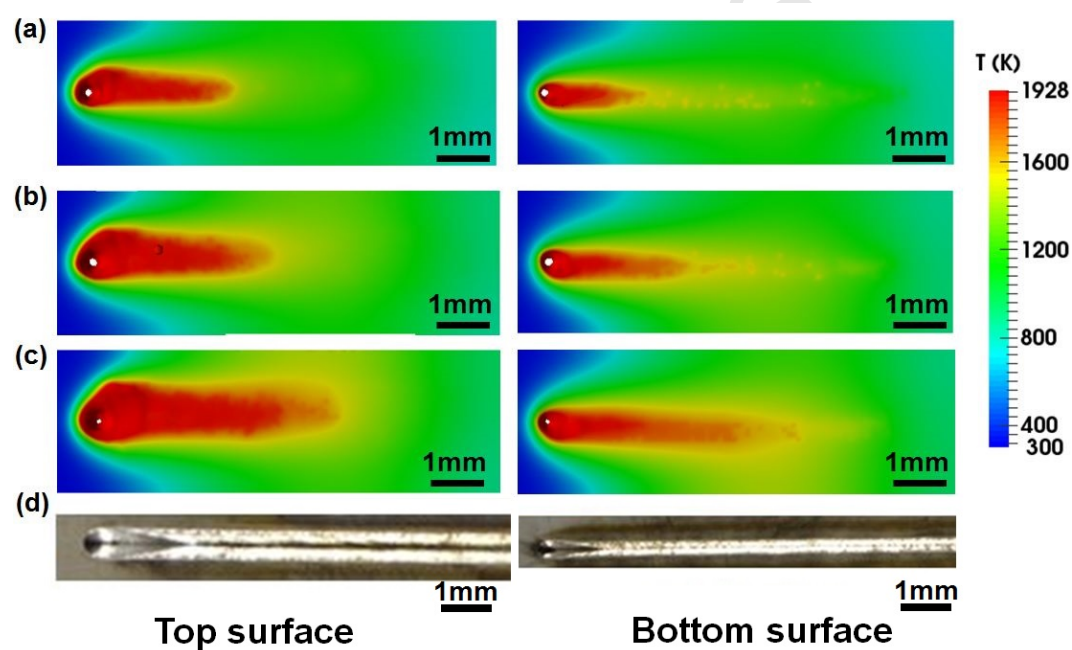


Figure 5: Captured weld pool shape using 2000W laser power and 100 mm/s welding speed at the top and bottom surfaces at (a) 200 μm , (b) 300 μm and (c) 400 μm beam radii of modelling results, compared with the same welding condition from experiment in (d).

weld pool shapes are qualitatively consistent with experimental observation at the same welding condition (Figure 5(d)).

A comparison of the predicted weld pool geometry against experimental measurements from a 1mm thick plate weld produced by a 2000W laser power and 100mm/s travel speed is shown in Fig. 6. The predictions shown in terms of the temperature profile are in good agreement with the measured weld pool shape. The study of thermal fluid flow induced porosity in full-penetration welds is

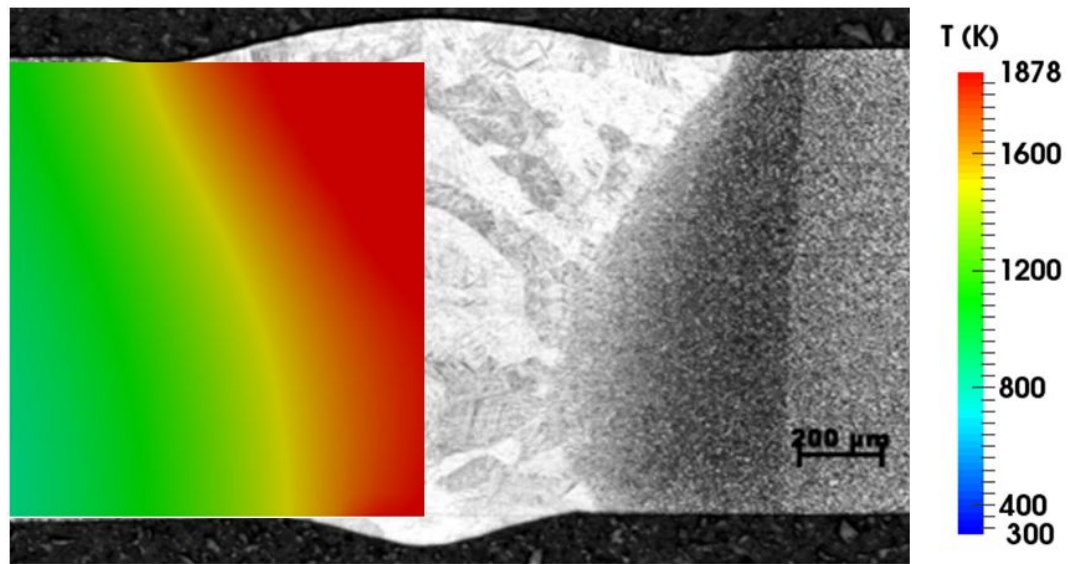


Figure 6: Cross section of fusion zone produced from the laser welding with the condition of $400\mu\text{m}$ beam radius and 2000 W laser power: comparison between predicted temperature profile in the fully developed weld pool and optical micrograph.

rather limited. Usually, porosity modelling concentrates on partial penetration welds with a stationary heat source to understand the keyhole collapse or shrinkage that was believed to induce the porosity in the condition representative to welding application (Panwisawas et al., 2017). A cross-section from the weld reveals that for this welding condition (2mm thick weld plate with 200mm/s travel speed and 4000W laser power) causes a full-penetration weld bead and the likely location of porosity has been predicted. After a welding time of 0.4 s

the solidification front has passed by the formed pore and it can be seen that a fluid flow induced pore has been encapsulated within the weld as seen from the solid fraction prediction in Fig.7(a). This corresponds with the most likely site of porosity which was reported to be in the lower part of the weld bead as demonstrated experimentally by Panwisawas et al. (2017) in Fig. 7(b).

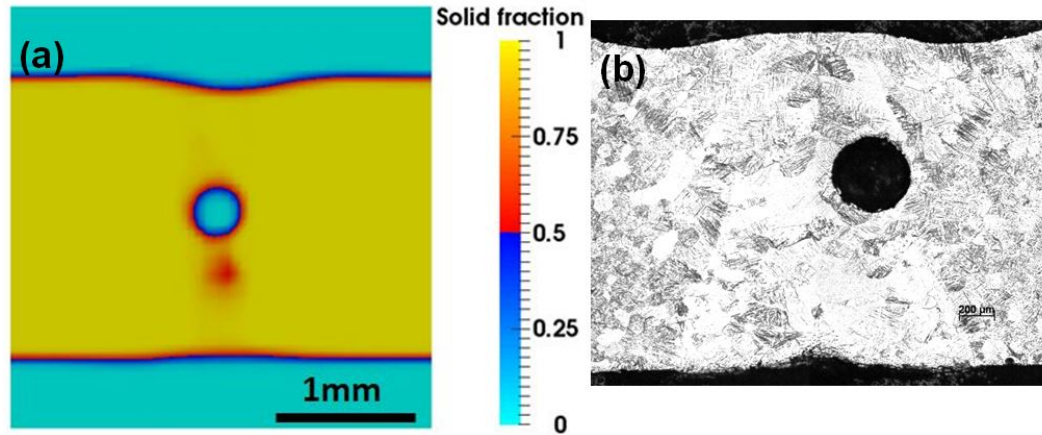


Figure 7: Porosity prediction from (a) the keyhole model using welding condition of 2mm weld thickness, 25 mm/s weld speed and 4000 W laser power, compared with (b) available experimental data of laser weld using the same condition (Panwisawas et al., 2017).

5. Conclusions

- The computational fluid dynamics model developed has been demonstrated to be capable of predicting keyhole dynamics, resulting weld pool geometry, keyhole interface evolution and temperature history, which are required for multi-scale modelling.
- Keyhole formation, keyhole oscillation, and concomitant melt pool dynamics are physically captured using the model. The modelling results of captured weld pool shape, melting front and process-induced porosity are in the same trend as available experimental information.

- Phase transition of the metallic component from liquid to vapour has played an important role governing the formation and stability of the keyhole.
- Porosity due to thermal fluid dynamics can be predicted from the model if the welding conditions are suitable for a pore to form. This is partly caused by the high flow velocity swirling down the keyhole front and vortex together with re-circulation flow at the toe of the weld bead.

Acknowledgments

C.P., Y.S., R.T., J.B and H.B acknowledges support by Centre for Advanced Simulation and Modelling collaborative project between Rolls-Royce plc, Manufacturing Technology Centre, University of Birmingham and part funded by the European Regional Development Fund with the grant number 080/P1/010. Professor Håkan Nilsson of Chalmers University of Technology as well as Professor Hrvoje Jasak of University of Zagreb and WIKKI Ltd. are gratefully acknowledged for detailed discussion about OpenFOAM coding and thermal fluid flow simulation.

References

- Abt, F., Boley, M., Weber, R., Graf, T., Popko, G., Nau, S., 2011. Novel x-ray system for in-situ diagnostics of laser based processes - first experimental results. *Physics Procedia* 12, 761–770.
- Boivineau, M., Cagran, C., Doytier, D., Eyraud, V., Nadal, M.H., Wilthan, B., Pottlacher, G., 2006. *International Journal of Thermophysics* 27, 507–529.
- Brackbill, J., Kothe, D., Zemach, C., 1992. A continuum method for modeling surface tension. *Journal of Computational Physics* 100, 335–354.
- Courtois, M., Carin, M., Masson, P.L., Gaied, S., Balabane, M., 2013. A new approach to compute multi-reflections of laser beam in a keyhole for heat

- transfer and fluid flow modelling in laser welding. *Journal of Physics D: Applied Physics* 46, 505305.
- Elmer, J., Palmer, T., Babu, S., Zhang, W., DebRoy, T., 2004. Phase transformation dynamics during welding of Ti-6Al-4V. *Journal of Applied Physics* 95, 8327–8339.
- Fabbro, R., 2010. 1 ed.. Woodhead Publishing Limited, New York. volume 1. chapter 8. pp. 211–241.
- Geiger, M., Leitz, K.H., Kock, H., Otto, A., 2009. A 3d transient model of keyhole and melt pool dynamics in laser beam welding applied to the joining of zinc coated sheets. *Prod. Eng. Res. Devel* 3, 127–136.
- Huang, J.L., Warnken, N., Gebelin, J.C., Strangwood, M., Reed, R.C., 2012. On the mechanism of porosity formation during welding of titanium alloys. *Acta Materialia* 60, 3215–3225.
- Jin, X., Li, L., Zhang, Y., 2002. A study on fresnel absorption and reflections in the keyhole in deep penetration laser welding. *Journal of Physics D: Applied Physics* 35, 2304–2310.
- Koch, H., Kägeler, C., Otto, A., Schmidt, M., 2011. Analysis of welding zinc coated steel sheets in zero gap configuration by 3d simulations and high speed imaging. *Physics Procedia* 12, 428–436.
- Landau, L.D., Lifshitz, E.M., 2010. *Fluid Mechanics*. volume 6. 2 ed., Elsevier Butterworth Heinemann, Oxford.
- Lee, J.Y., h. Ko, S., Farson, D.F., Yoo, C.D., 2002. Mechanism of keyhole formation and stability in stationary laser welding. *Journal of Physics D: Applied Physics* 35, 1570–1576.
- Li, J.Z., Johnson, W.L., Rhim, W.K., 2006. *Applied Physics Letter* 89, 111913.

- Otto, A., Koch, H., Leitz, K.H., Schmidt, M., 2011. Numerical simulations - a versatile approach for better understanding dynamics in laser material processing. *Physics Procedia* 12, 11–20.
- Panwisawas, C., Perumal, B., ward, R., Turner, N., turner, R.P., Brooks, J.W., Basoalto, H.C., 2017. Keyhole formation and thermal fluid flow-induced porosity during laser fusion welding in titanium alloys: Experimental and modelling. *Acta Materialia* 126, 251–263.
- Rai, R., Burgardt, P., Mileewski, J., Lienert, T., DebRoy, T., 2009a. Heat transfer and fluid flow during electron beam welding of 21cr-6ni-9mn steel and ti-6al-4v alloy. *Journal of Physics D: Applied Physics* 42, 025503(12pp).
- Rai, R., Elmer, J., Palmern, T., DebRoy, T., 2007. Heat transfer and fluid flow during keyhole mode laser welding of tantalum, ti-6al-4v, 304l stainless steel and vanadium. *Journal of Physics D: Applied Physics* 40, 5753–5766.
- Rai, R., Palmer, T.A., Elmer, J., DebRoy, T., 2009b. Keyhole modeling during laser welding. *Welding Research* 88, 54–61.
- Rösler, F., Brüggemann, D., 2011. Shell-and-tube type latent heat thermal energy storage: numerical analysis and comparison with experiments. *Heat Mass Transfer* 47, 1027–1033.
- Saldi, Z.S., 2012. Marangoni driven free surface flows in liquid weld pools. Ph.D. thesis. Delft University of Technology. Department of Multiscale Physics, Faculty of Applied Sciences, Delft University of Technology, Prinsbernhardlaan 6, 2628 BW, Delft, The Netherlands.
- Scriven, L.E., Sternling, C.V., 1960. The marangoni effects. *Nature* 187, 186–188.
- Sun, Y., Beckermann, C., 2004. Diffuse interface modeling of two-phase flows based on averaging: mass and momentum equations. *Physica D* 198, 281–308.

- Svenungsson, J., Choquet, I., Kaplan, A., 2015. Laser welding process - a review of keyhole modelling. *Physics Procedia* 78, 182–191.
- Tan, W., Bailey, N.S., Shin, Y.C., 2013. Investigation of keyhole plume and molten pool based on a three-dimensional dynamic model with sharp interface formulation. *Journal of Physics D: Applied Physics* 46, 055501.
- Tan, W., Shin, Y.C., 2015. Multi-scale modeling of solidification and microstructure development in laser keyhole welding process for austenitic stainless steel. *Computational Materials Science* 98, 446–458.
- Voller, V.R., Cross, M., Markatos, N.C., 1987. An enthalpy method for convection/diffusion phase change. *International Journal for Numerical Methods in Engineering* 24, 271–284.
- Xu, G.X., Wu, C.S., Qin, G.L., Wang, X.Y., Lin, S.Y., 2011. Adaptive volumetric heat source models for laser beam and laser + pulsed GMAW hybrid welding processes. *Int J Adv Manuf Technol* 57, 245–255.
- Ytrehus, T., Østomo, S., 1996. Kinetic theory approach to interphase processes. *Int. J. Multiphase Flow* 22, 133–155.
- Zhang, M., Chen, G., Zhou, Y., Li, S., 2013. Direct observation of keyhole characteristics in deep penetration laser welding with a 10 kw fiber laser. *Optics Express* 21, 19997–20004.
- Zhao, H., Niu, W., Zhang, B., Lei, Y., Kodama, M., Ishide, T., 2011. Modelling of keyhole dynamics and porosity formation considering the adaptive keyhole shape and three-phase coupling during deep-penetration laser welding. *Journal of Physics D: Applied Physics* 44, 485302.

Figure captions

1. Figure 1: Keyhole formation and time to full penetration of the laser welding with different beam radii: (a) $200\mu\text{m}$, (b) $300\mu\text{m}$, and (c) $400\mu\text{m}$.
2. Figure 2: Keyhole oscillation and fully developed weld pool formation of the laser welding with $400\mu\text{m}$ beam radius and 2000 W laser power.
3. Figure 3: Comparison of captured weld pool shape and melting front: (a) modelling results illustrating the weld pool and incompletely collapsed keyhole qualitatively compared with available X-ray tomography results from fusion weld (b), after Huang et al. (2012), and longitudinal section illustrating the captured melting front from (c) fraction of solid result from modelling, qualitatively compared with the same experiment (d) after Huang et al. (2012).
4. Figure 4: Weld pool dynamics of the steady state weld pool shapes during the laser welding of 2000 W laser power with different beam radii. The results show (a) fluid flow around the keyhole, (b) longitudinal view of weld pool and (c) top view of the melt pool.
5. Figure 5: Captured weld pool shape using 2000W laser power and 100 mm/s welding speed at the top and bottom surfaces at (a) $200\mu\text{m}$, (b) $300\mu\text{m}$ and (c) $400\mu\text{m}$ beam radii of modelling results, compared with the same welding condition from experiment in (d).
6. Figure 6: Cross section of fusion zone produced from the laser welding with the condition of $400\mu\text{m}$ beam radius and 2000 W laser power: comparison between predicted temperature profile in the fully developed weld pool and optical micrograph.
7. Figure 7: Porosity prediction from (a) the keyhole model using welding condition of 2mm weld thickness, 25 mm/s weld speed and 4000 W laser power, compared with (b) available experimental data of laser weld using the same condition (Panwisawas et al., 2017).

Table captions

1. Table 1: Chemical composition of Ti-6Al-4V material used in this work (weight percentage).
2. Table 2: Data used for fluid flow and heat transfer calculations reported by Li et al. (2006); Rai et al. (2007, 2009a).
3. Table 3: Data used for heat source model in this calculation.